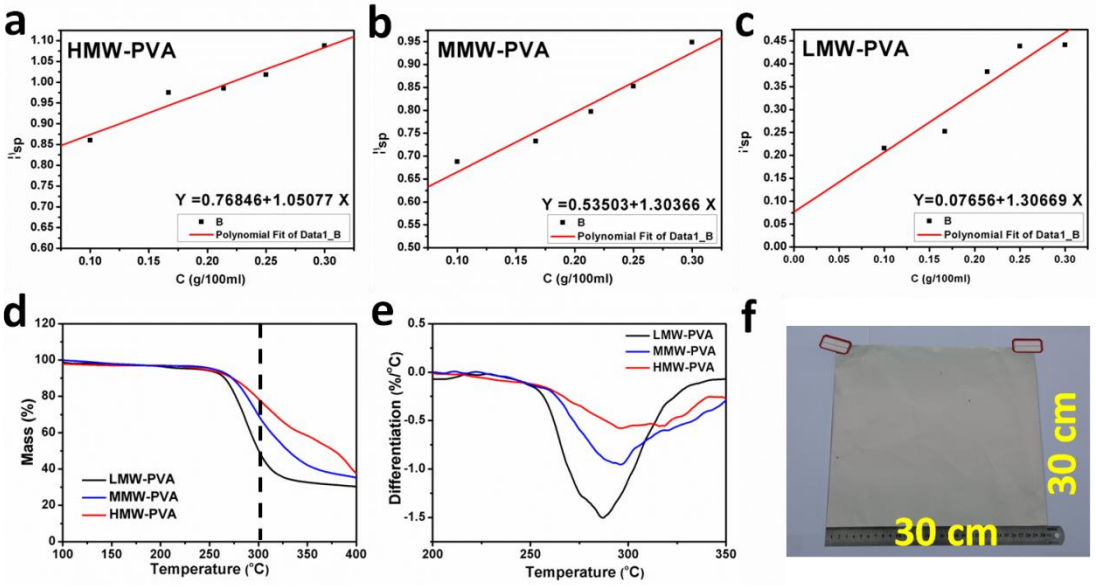


**g**

| | 25℃, K=0.0002, α=0.76, [η]=K*M$^{\alpha}$ | | |
|---|---|---|---|
| | **[η] (dL/g)** | **$M_{\eta}$** | **γ (mN/m)** |
| **HMW-PVA** | 0.76846 | 52067 | 51.4 |
| **MMW-PVA** | 0.53503 | 32334 | 41.6 |
| **LMW-PVA** | 0.07656 | 2504 | 40.1 |
| **PVP(K13~18)** | 0.01350 | 323 | 30.0 |

**Supplementary Figure 1 | a-c**, The viscosity fitting curves of high-molecular-weight poly(vinyl alcohol) (HMW-PVA) (**a**), middle-molecular-weight poly(vinyl alcohol) (MMW-PVA) (**b**) and low-molecular-weight poly(vinyl alcohol) (LMW-PVA) (**c**). **d**, TG curves of these three samples in air. **e**, The differential of the mass loss and temperature. **f**, Photograph of the aluminum foil after electrospinning for 8 h with one ordinary syringe needle. The area is ~900 $cm^2$. **g**, The viscosity-averaged molecular weights of HMW-PVA, MMW-PVA, LMW-PVA and PVP (K13~18).

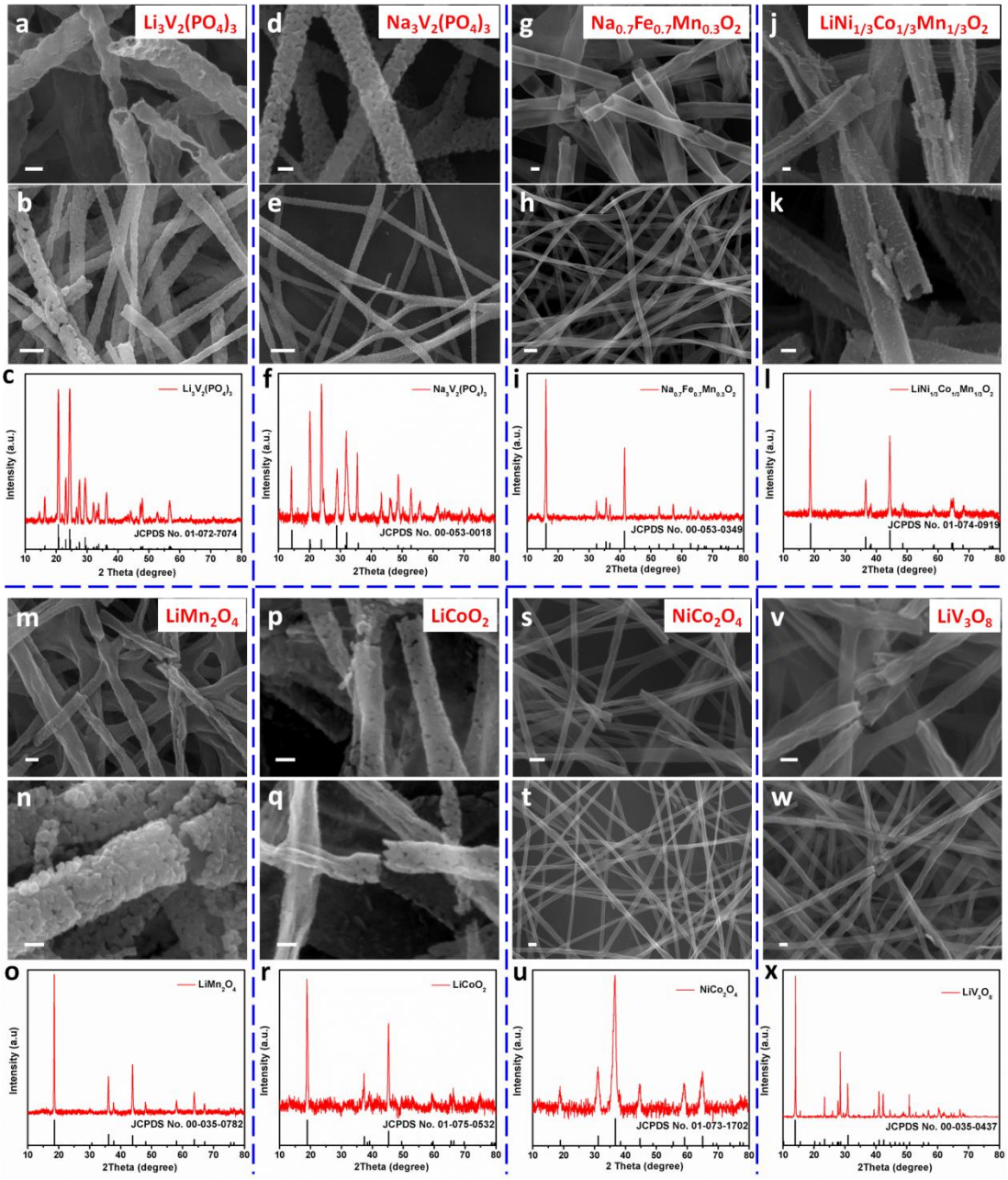


**Supplementary Figure 2 |** SEM images and XRD patterns of multi-element oxides, $Li_3V_2(PO_4)_3$ (**a-c**), $Na_3V_2(PO_4)_3$ (**d-f**), $Na_{0.7}Fe_{0.7}Mn_{0.3}O_2$ (**g-i**), and $LiNi_{1/3}Co_{1/3}Mn_{1/3}O_2$ (**j-l**), and binary-metal oxides $LiMn_2O_4$ (**m-o**), $LiCoO_2$ (**p-r**), $NiCo_2O_4$ (**s-u**), and $LiV_3O_8$ (**v-x**) mesoporous nanotubes. The scale bar in **b**, **e** and **h** is 500 nm, the rest is 100 nm.

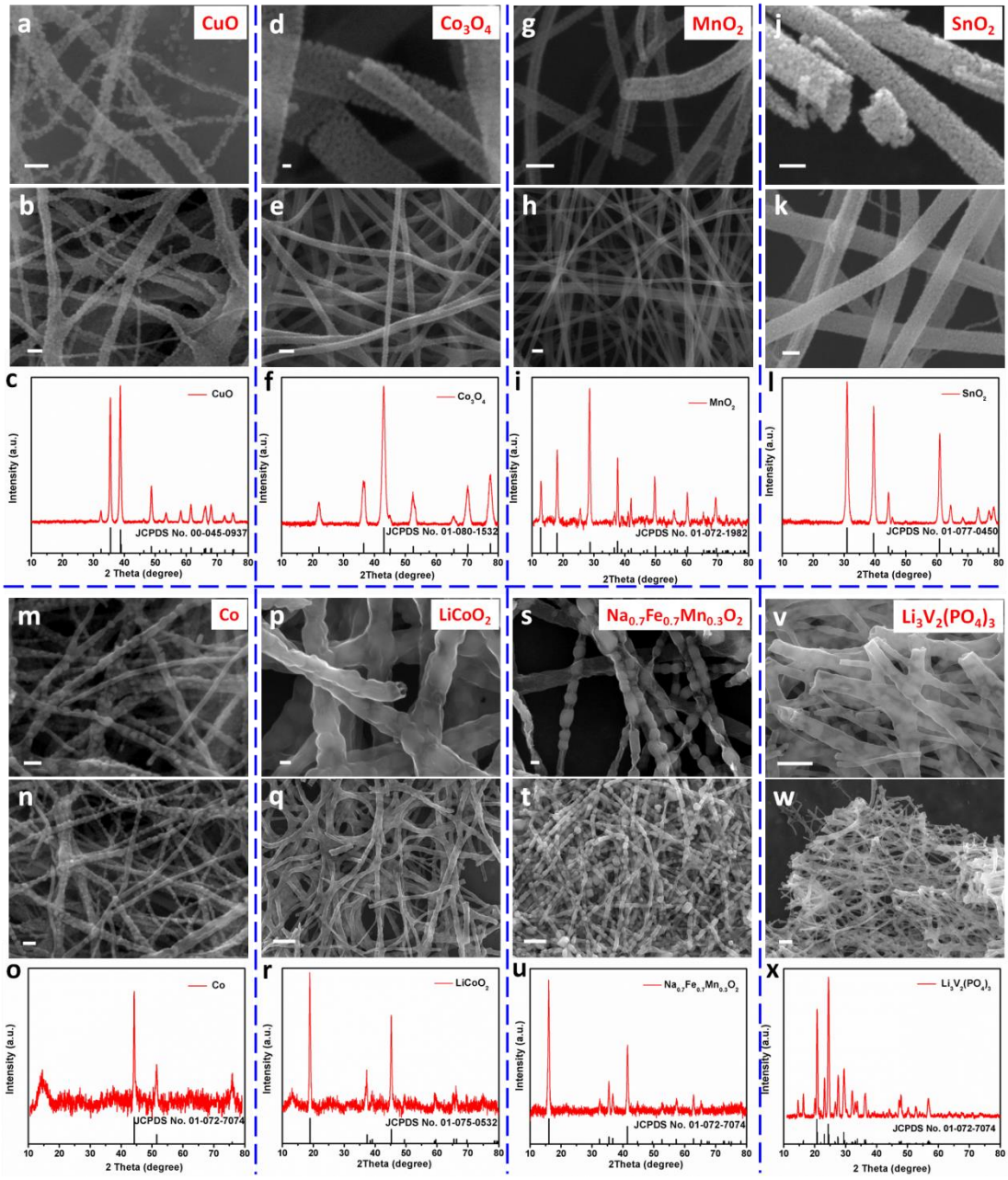


**Supplementary Figure 3 |** SEM images and XRD patterns of single-metal oxides mesoporous nanotubes, CuO (**a-c**), $Co_3O_4$ (**d-f**), $MnO_2$ (**g-i**), and $SnO_2$ (**j-l**), and pea-like nanotubes which are selected from different species, Co (**m-o**), $LiCoO_2$ (**p-r**), $Na_{0.7}Fe_{0.7}Mn_{0.3}O_2$ (**s-u**) and $Li_3V_2(PO_4)_3$ (**v-x**). The scale bar in **q**, **t, v** and **w** is 1 μm, the rest is 100 nm.

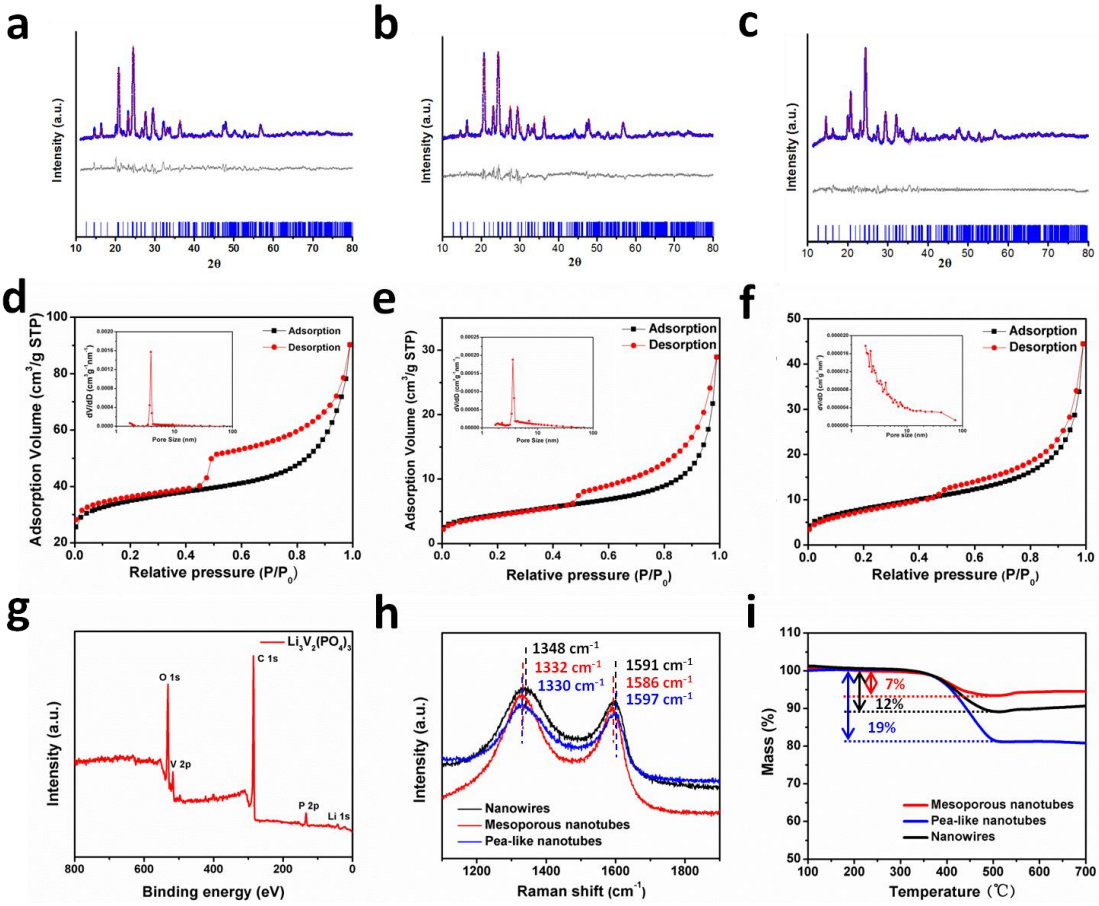


**Supplementary Figure 4 | a-c**, Profile fitting plots of $Li_3V_2(PO_4)_3$ mesoporous nanotubes (**a**), pea-like nanotubes (**b**) and nanowires (**c**). The crystal sizes of the $Li_3V_2(PO_4)_3$ mesoporous nanotubes, pea-like nanotubes and nanowires are 33.8, 106.8 and 22.3 nm, respectively, according to Rietveld analysis results; these sizes are consistent with those observed in SEM and TEM images. The XRD patterns are indexed to a monoclinic structure (JCPDS No. 01-072-7074). **d-f**, $N_2$ adsorption-desorption isotherms and pore size distribution curves (inset) for $Li_3V_2(PO_4)_3$ mesoporous nanotubes (**d**), pea-like nanotubes (**e**) and nanowires (**f**). The specific areas of these samples are 115, 33 and 15 $m^2/g$, respectively. **g**, X-ray photoelectron spectrum (XPS) of the $Li_3V_2(PO_4)_3$ mesoporous nanotube surface. **h-i**, Raman spectra (**h**) and TG curves (**i**) of $Li_3V_2(PO_4)_3$ mesoporous nanotubes, pea-like nanotubes and nanowires.

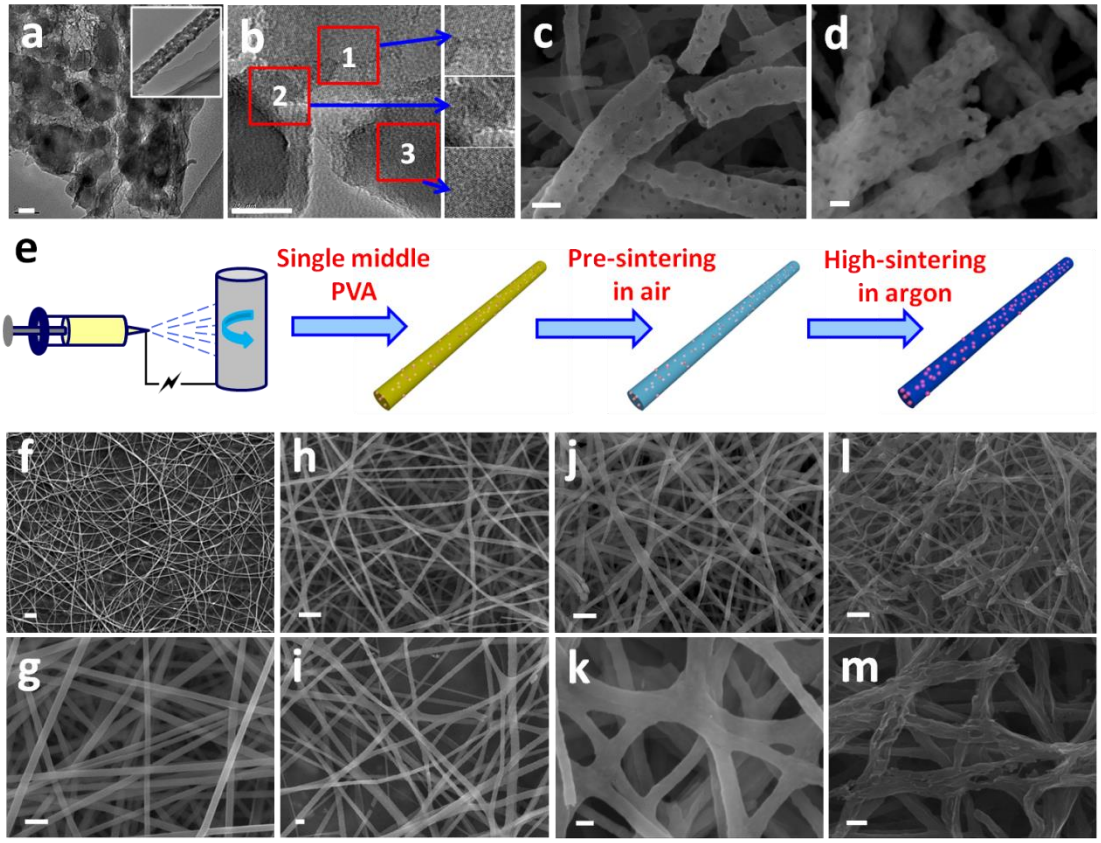


**Supplementary Figure 5 | a-b**, TEM (**a**) and high-resolution TEM (**b**) images of $Li_3V_2(PO_4)_3$ mesoporous nanotubes with scale bar at 20 nm. The inset of (**a**) is TEM image of one $Li_3V_2(PO_4)_3$ mesoporous nanotube. **c**, SEM image of $Li_3V_2(PO_4)_3$ mesoporous nanotubes pre-sintered at 300 °C for 10 h in air with scale bar at 100 nm. **d**, SEM images of $Li_3V_2(PO_4)_3$ mesoporous nanotubes pre-sintered at 350 °C for 10 h in air to remove additional PVA, getting larger pores on the nanotubes. The scale bar is 100 nm. **e**, Schematic diagram of electrospinning composite nanowires with only middle-molecular-weight PVA. **f-g**, SEM images of composite nanowires after electrospinning. **h-i**, SEM images of composite nanowires pre-sintered at 300 °C for 3 h in air. **j-k**, SEM images of $Li_3V_2(PO_4)_3$ nanowires subjected to high-temperature sintering at 800 °C for 3 h under argon. **l-m**, SEM images of carbon nanowires after removal of $Li_3V_2(PO_4)_3$ with hydrogen fluoride. The scale bar is 1μm in **f**, **h**, **j**, **l** and 200 nm in **g**, **i**, **k**, **m**. As a control sample, $Li_3V_2(PO_4)_3$ nanowires were also electrospun with only middle-molecular-weight PVA. First, the uniform precursor solution for electrospinning was prepared with 1.6 mol of middle-molecular-weight PVA and 20 ml of deionized water. Then, LiOH, $NH_4VO_3$ and $NH_4H_2PO_4$ were added in a molar ratio of 3:2:3. After being electrospun, the composite nanowires were annealed at 300 °C in air for 3 h, leading to pyrolysis of the middle-weight PVA. They were subsequently annealed at 800 °C under an argon atmosphere for 6 h.

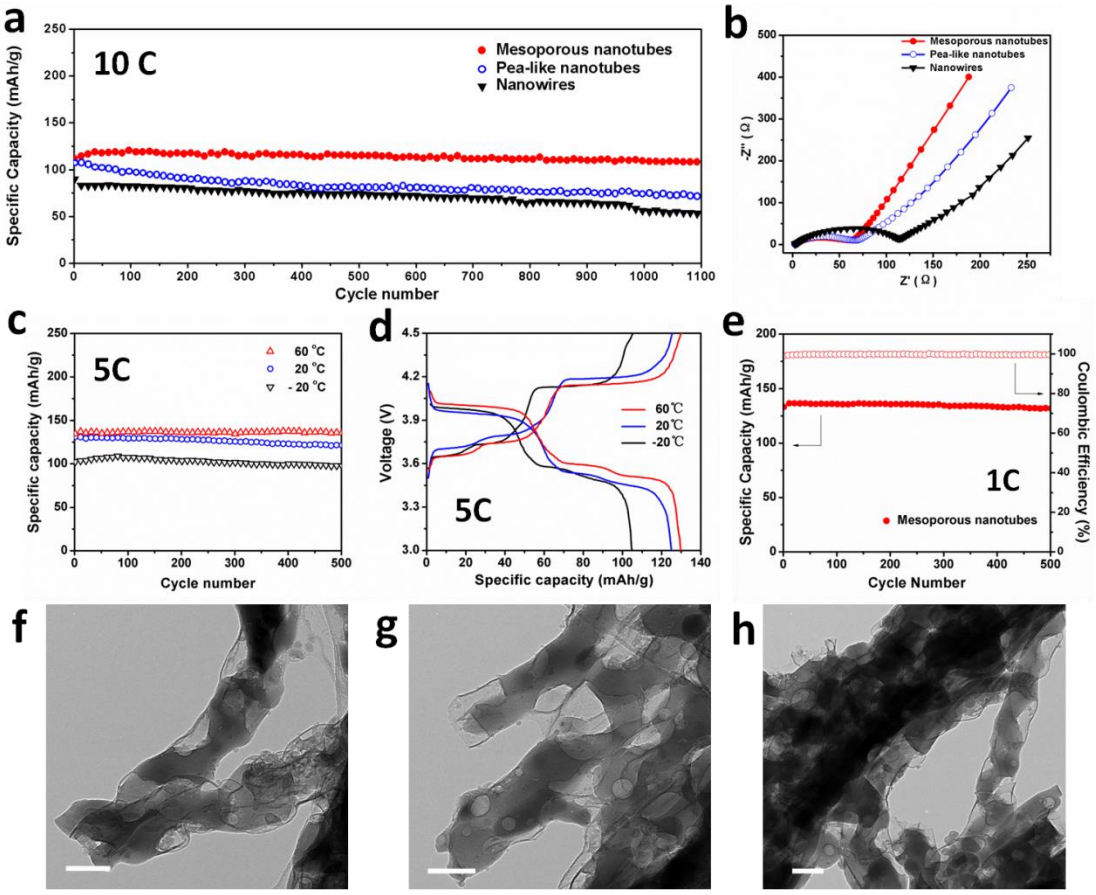


**Supplementary Figure 6 | Electrochemical performance of $Li_3V_2(PO_4)_3$ nanowires, mesoporous nanotubes and pea-like nanotubes in lithium half-cells. a**, Cycling performance of the half-cells measured at 10 C. **b**, AC impedance plots of these three samples. **c-d**, Cycling performance and charge-discharge curves collected at a rate of 5 C at temperatures of -20, 20 and 60 °C, respectively. **e**, Cycling performance and the corresponding coulombic efficiency measured at 1 C for 500 cycles. **f-h**, TEM images of $Li_3V_2(PO_4)_3$ mesoporous nanotubes after cycling 5000 times at the rate of 10 C with scale bar at 100 nm. At the high current density of 10 C, $Li_3V_2(PO_4)_3$ nanowires, mesoporous nanotubes and pea-like nanotubes deliver initial discharge capacities of 112, 107 and 90 mAh/g, respectively, after 1,100 cycles, the corresponding capacity retentions were 99%, 71% and 68%, respectively.

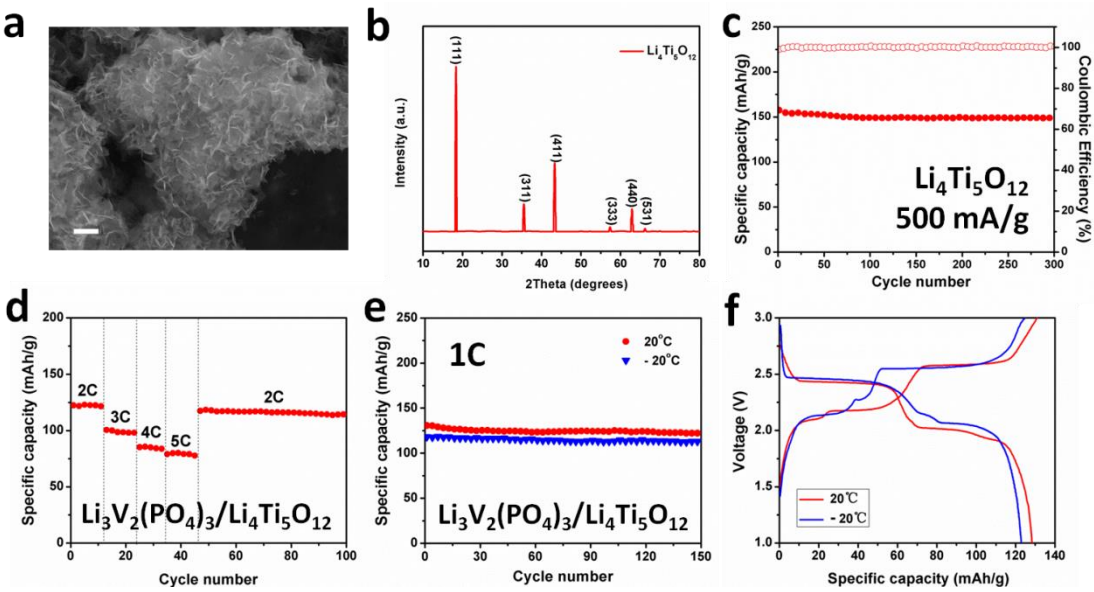


**Supplementary Figure 7 | Electrochemical performance of $Li_3V_2(PO_4)_3/Li_4Ti_5O_{12}$ full batteries. a-b**, SEM image (**a**) of $Li_4Ti_5O_{12}$ nanosheets with scale bar at 1μm, and the corresponding XRD pattern (**b**). **c**, Cycling performance of $Li_4Ti_5O_{12}$ nanosheets measured at 500 mA/g in a lithium half-cell. **d**, Specific capacity measurements at 20 °C of the $Li_3V_2(PO_4)_3/Li_4Ti_5O_{12}$ full battery at different rates ranging from 2 to 5 C. **e-f**, Cycling performance (**e**) and charge/discharge curves (**f**) of the $Li_3V_2(PO_4)_3/Li_4Ti_5O_{12}$ full batteries measured at a rate of 1 C and at temperatures of -20 °C and 20 °C. $Li_4Ti_5O_{12}$ half cell exhibited stable cycling performance and coulombic efficiency when measured at a rate of 500 mA/g. The $Li_3V_2(PO_4)_3/Li_4Ti_5O_{12}$ lithium-ion full batteries exhibited the initial capacities of 130 and 118 mAh/g when tested at temperatures of 20 °C and -20 °C, respectively, showing stable cycling performance at both room and low temperature.

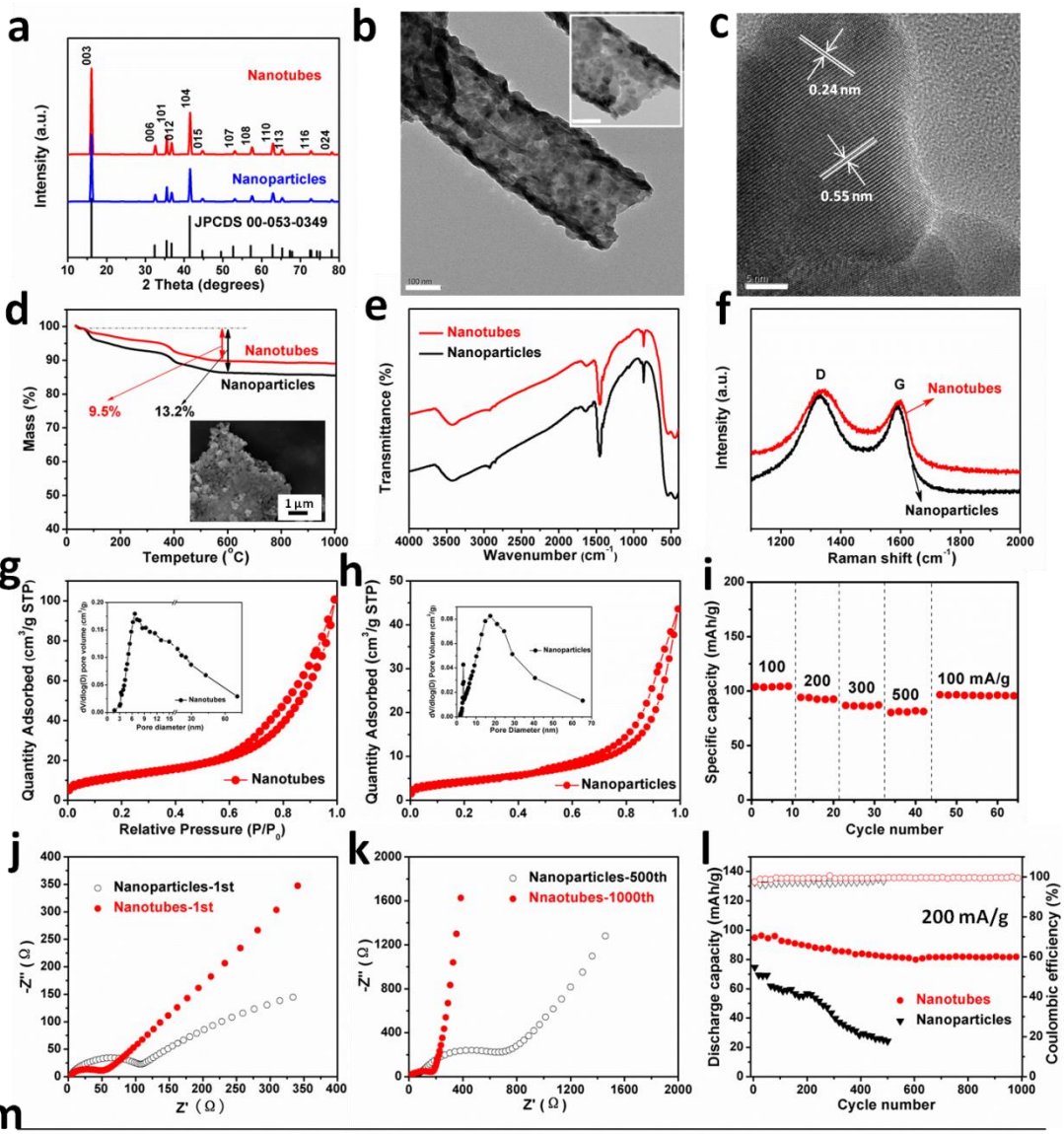


m

| | | Voltage range (V) | Current density (mA/g) | Initial Capacity (mAh/g) | Cycle number | Capacity fading per cycle | Reference |
|---|---|---|---|---|---|---|---|
| 1 | $Na_{0.7}Fe_{0.7}Mn_{0.3}O_2$ | 3.0-4.5 | 100 | 108 | 1000 | 0.0105% | Our work |
| | | | 500 | 82 | 5000 | 0.0071% | |
| 2 | P2-$Na_{2/3}Fe_{1/2}Mn_{1/2}O_2$ | 1.5-4.2 | 13 | 190 | 30 | 0.78% | *Nat. Mater.*, 11 (7), 512 (2012) |
| 3 | P2-$Na_{2/3}Fe_{1/2}Mn_{1/2}O_2$ | 1.5-4.2 | 26 | 195 | 80 | 0.19% | *ACS Appl. Mater. Inter.*, 6, 8953 (2014). |
| 4 | P2-$Na_{1.0}Li_{0.2}Ni_{0.25}Mn_{0.75}O_2$ | 2.0-4.2 | 15 | 128 | 50 | 0.26% | *Chem. Mater.*, 26, 1260 (2014) |
| 5 | $Na[Ni_{0.25}Fe_{0.5}Mn_{0.25}]O_2$ | 2.1-3.9 | 130 | 133 | 50 | 0.30% | *Nano Lett.*, 14 (3), 1620 (2014) |

**Supplementary Figure 8 | Characterization and electrochemical performance of $Na_{0.7}Fe_{0.7}Mn_{0.3}O_2$ mesoporous nanotubes and nanoparticles in sodium-ion batteries. a**, XRD patterns of $Na_{0.7}Fe_{0.7}Mn_{0.3}O_2$ mesoporous nanotubes and nanoparticles. **b**, TEM images of $Na_{0.7}Fe_{0.7}Mn_{0.3}O_2$ mesoporous nanotubes with scale bar at 100 nm. **c**, High-resolution TEM image of $Na_{0.7}Fe_{0.7}Mn_{0.3}O_2$ mesoporous nanotubes with scale bar at 5 nm. **d-f**, TG curves (**d**), FT-IR spectra (**e**) and Raman spectra (**f**) of the materials. **g-h**, $N_2$ adsorption-desorption isotherms and

pore size distribution curves (inset) of $Na_{0.7}Fe_{0.7}Mn_{0.3}O_2$ mesoporous nanotubes (**g**) and nanoparticles (**h**). **i**, Rate performance tested at 100, 200, 300 and 500 mA/g. **j-k**, AC impedance plots at the first cycle (**j**), 500$^{th}$ cycle and 1000$^{th}$ cycle (**k**). **l**, Cycling performance at 200 mA/g. **m**, A comparison of the electrochemical properties of the $Na_{0.7}Fe_{0.7}Mn_{0.3}O_2$ prepared in this work with those of the materials reported in the literatures. The HRTEM image displays lattice fringes with *d*-spacings of 0.55 and 0.24 nm, which correspond to the (003) and (012) planes, respectively, of the rhombohedral $Na_{0.7}Fe_{0.7}Mn_{0.3}O_2$ crystal. At the same time, compared with $Na_{0.7}Fe_{0.7}Mn_{0.3}O_2$ nanoparticles, which were synthesized as a control sample, $Na_{0.7}Fe_{0.7}Mn_{0.3}O_2$ mesoporous nanotubes exhibit much better electrochemical performance. The carbon mass content of $Na_{0.7}Fe_{0.7}Mn_{0.3}O_2$ mesoporous nanotubes is only 9.5%, which is smaller than nanoparticles (13.2%), but mesoporous nanotubes reveal larger specific surface area (95 $m^2/g$) than nanoparticles (15 $m^2/g$), which can greatly enhance the electrode-electrolyte contact area.

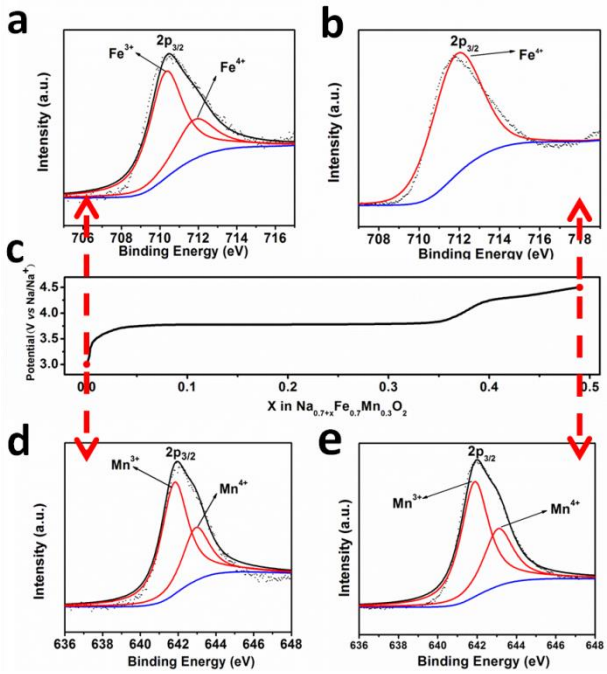


**Supplementary Figure 9 | a-b**, X-ray photoelectron spectra and Fe $2p_{3/2}$ curve fits for the original $Na_{0.7}Fe_{0.7}Mn_{0.3}O_2$ mesoporous nanotubes surface (**a**) and for the material charged to 4.5 V (**b**). **c**, Evolution of the cell voltage as a function of the sodium content in $Na_{0.7+x}Fe_{0.7}Mn_{0.3}O_2$ over the $0 \leq x \leq 0.49$ composition range. **d-e**, X-ray photoelectron spectra and Mn $2p_{3/2}$ curve fits for the original $Na_{0.7}Fe_{0.7}Mn_{0.3}O_2$ mesoporous nanotube surface (**d**) and for the material charged to 4.5 V (**e**). This measurement clearly demonstrates that the discharge capacity of $Na_{0.7}Fe_{0.7}Mn_{0.3}O_2$ mesoporous nanotubes mainly comes from the contribution of iron element.

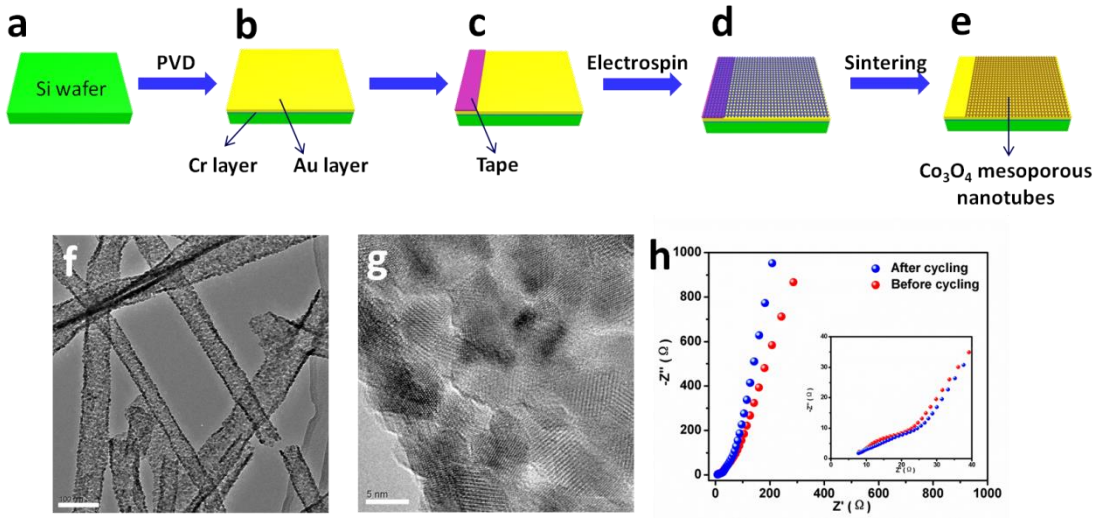


**Supplementary Figure 10 | a-e**, Schematic of the fabrication process for a $Co_3O_4$ mesoporous nanotube based device integrated onto a silicon wafer. **a**, The cleaned silicon wafer. **b**, The chromium layer (~5 nm) and gold layer (~50 nm) deposited on the silicon wafer using physical vapor deposition (PVD). **c**, Tape placed on the surface of one side. **d**, Electrospinning of $Co_3O_4$ onto the surface. **e**, Tape removal and sintering at 350 °C in air for 5 h to acquire a layer of $Co_3O_4$ mesoporous nanotubes on the surface. The thickness of the $Co_3O_4$ mesoporous nanotubes was ~850 nm. **f-g**, TEM images of the resulting $Co_3O_4$ mesoporous nanotubes. **h**, AC impedance plots of the $Co_3O_4$ mesoporous nanotubes based supercapacitor. The inset is a magnified plot of the high-frequency region.